Three-Dimensional Conformation of Folded Polymers in Single Crystals

You-lee Hong,[1] Shichen Yuan,[1] Zhen Li,[1] Yutian Ke,[1] Koji Nozaki,[2] and Toshikazu Miyoshi[1,*]

[1]*Department of Polymer Science, The University of Akron, Akron, Ohio 44325, USA*
[2]*Department of Physics, Graduate School of Science and Engineering Yamaguchi University, Yamaguchi 753-8512, Japan*

The chain-folding mechanism and structure of semicrystalline polymers have long been controversial. Solid-state NMR was applied to determine the chain trajectory of ^{13}C CH$_3$-labeled *isotactic* poly(1-butene) (*i*PB1) in form III chiral single crystals blended with nonlabeled *i*PB1 crystallized in dilute solutions under low supercooling. An advanced ^{13}C-^{13}C double-quantum NMR technique probing the spatial proximity pattern of labeled ^{13}C nuclei revealed that the chains adopt a three-dimensional (3D) conformation in single crystals. The determined results indicate a two-step crystallization process of (i) cluster formation via self-folding in the precrystallization stage and (ii) deposition of the nanoclusters as a building block at the growth front in single crystals.

                                                     PACS numbers: 82.35.Lr, 36.20.-r, 87.15.nt

The crystallization of polymers and small molecules is commonly described in terms of nucleation and growth [1], in which primary nucleation produces three-dimensional (3D) nuclei to minimize surface free energy and subsequent secondary nucleation and growth on the existing crystals dominate the crystallization process. Chain folding in polymer crystals leads to complexity in the crystallization process and has thus motivated theoretical and experimental studies over the last half century.

The well-developed Lauritzen and Hoffman (LH) theory describes secondary nucleation and growth as sequential stem deposition on the growth front driven by kinetics [2,3]. The LH theory predicts that sufficiently low supercooling leads to a well-ordered linear arrangement of the folded chains (2D conformation) on the growth front, as illustrated in route (a) of Fig. 1. Conversely, Allegra *et al.* have turned their attention to a metastable bundle structure (3D conformation) in which 4–20 stems aggregate during a precrystallization stage in dilute solutions [4]. Muthukumar *et al.* simulated the generation of nuclei by single chains via self-folding in dilute solutions [5–7]. Based on the bundle formation, we considered entire molecules or portions of molecules that form preordered objects with 3D structures at an early stage and are subsequently deposited at the growth front during later stages [route (b) in Fig. 1]. Thus, surface-induced folding and self-folding lead to substantially different conformations (2D as opposed to 3D) for the folded chains in solution-grown crystals.

Over the past several decades, various experimental techniques such as neutron scattering (NS) [8,9], infrared spectroscopy (IR) [10], decoration approach [11], and atomic force microscopy (AFM) [12–14] have been developed and used to characterize the chain-folding (CF) structure of polymers in melt- and solution-grown crystals. Nevertheless, detailed CF structures remain a matter of debate because of experimental limitations. In particular,

the determination of conformation of folded chains provides a critical clue for the crystallization process at molecular levels.

Solid-state NMR (SS-NMR) is a sophisticated technique for the structural and dynamic analysis of inorganic materials and organic molecules [15–21]. Among the various magnetic interactions, dipolar interactions, which are inversely proportional to the third power of the internuclear distance, have been successfully used to determine the local conformation and packing of polymers [15] and peptides [16,17], intermolecular interactions of self-assembly systems [18], and 3D structure of peptides [19] and proteins [20]. Recently, we proposed a strategy to investigate detailed CF structures in which the adjacent reentry sites, successive adjacent reentry number $\langle n \rangle$, and adjacent reentry fraction $\langle F \rangle$ are obtained from the analysis of ^{13}C-^{13}C double-quantum (DQ) buildup curves [21]. Such data are sensitive to the spatial arrangement of ^{13}C labels, and detailed information on the chain folding
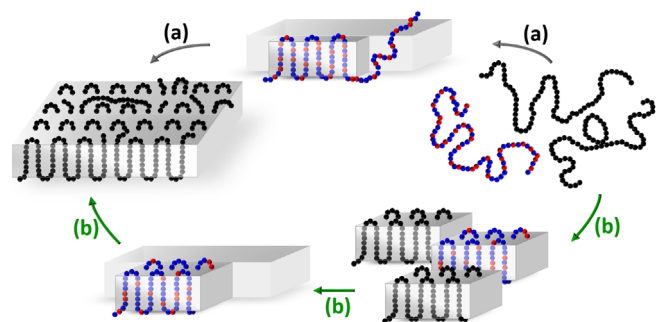
FIG. 1 (color online).   Schematic of polymer crystallization. (a) One-step: subsequent stem deposition on the surface of existing crystals. (b) Two-step: cluster formation via folding during the precrystallization stage and deposition of the clusters on the crystal surface. The ^{13}C-labeled chains and atoms are colored blue and red, respectively.

is obtained by comparison with data simulated on the basis of different models. This strategy was applied to ^{13}C CH$_3$-labeled *isotactic* poly(1-butene) (*i*PB1) form I ($M_w = 37$ Kg/mol) in solution-grown crystals as a function of crystallization temperature (T_c). Consequently, the *i*PB1 chains were observed to adopt adjacent reentry patterns with $\langle n \rangle \geq 8$ along (100) and (010) (zigzag pattern) under both low and high supercooling, whereas the crystal habits were highly dependent on T_c: high T_c induced hexagonal single crystals, whereas low T_c resulted in circular crystals [22,23]. These findings clearly indicate that kinetics differentially affect crystalline structures at different length scales. The T_c independence of the CF structure contradicts the kinetic theory hypothesis [2] and instead supports the existence of preordered objects such as bundles or clusters prior to crystal growth. Nevertheless, the possible formation of surface-induced 2D clusters could not be disproved because the linear zigzag CF pattern generated a single DQ curve similar to that of the 3D cluster. However, the 2D and 3D conformations of the folded labeled chains lead to characteristically different DQ data detected at different crystallographic sites. Therefore, an evaluation of the site-resolved NMR data would allow us to identify the conformations of the folded chains.

In this work, we aimed to elucidate the conformation of folded polymer chains in single crystals as well as to improve our understanding of polymer crystallization at the molecular level. The chiral form III of *i*PB1 with the same M_w as that used in our former work was chosen among various systems [23]. The asymmetric chiral packing structure of form III generates two magnetically inequivalent sites in each stem [24,25]. Dipolar interactions at the two inequivalent sites allowed us to investigate the conformation of the folded chains.

AFM demonstrated that the form III single crystal assumes a scrolled-tube morphology, as shown in Fig. 2(a), and the measured crystal thickness of a single layer was approximately 8.5 nm [Figs. S1(a) and S1(b)]. The measured thickness and average M_w indicated a maximum folding number $\langle n_{max} \rangle$ of 13.

The relaxation-filter technique ($T_{1\rho H}$: ^{1}H spin-lattice relaxation in the rotating frame) was used to suppress the amorphous signals [Fig. S2]. The ^{13}C filtered single-quantum (SQ) and DQ CPMAS NMR spectra of ^{13}C CH$_3$-labeled *i*PB1 form III single crystals are presented in Fig. 2(b) [26]. Figures 2(c) and 2(d) show the orthorhombic unit-cell structure of form III, with lattice dimensions of $a = 12.38 \pm 0.08$, $b = 8.88 \pm 0.06$, and $c = 7.56 \pm 0.05$ Å, with individual chains adopting a 4_1 helical conformation [29]. Figure 2(e) depicts the ^{13}C-^{13}C DQ efficiency (ξ) of ^{13}C-labeled CH$_3$ groups as a function of τ_{ex}. The maximum DQ efficiency (ξ_{max}) values at 15.1 and 14.2 ppm were 25% and 27%, respectively. DQ curves are determined by ^{13}C-^{13}C dipolar interactions, which are governed by the
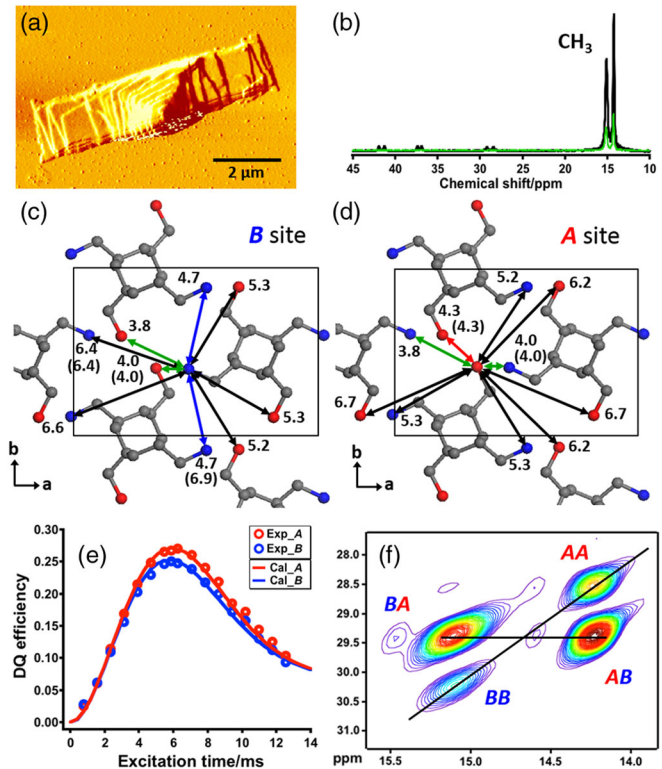
FIG. 2 (color online). (a) AFM amplitude error image of *i*PB1 form III crystallized at 50 °C. (b) ^{13}C $T_{1\rho H}$-filtered DQ (green) and SQ (black) spectrum of 35% ^{13}C-labeled *i*PB1 form III measured at −20 °C. Chain-packing structure of *i*PB1 form III on the (001) plane and ^{13}CH$_3$-^{13}CH$_3$ internuclear distances at (c) the *B* and (d) *A* sites colored blue and red, respectively. The unit for all distances is Å. The numbers in parentheses indicate the distance between the overlapping carbons with different z coordinates on the (001) plane. (e) Experimental (open circles) ξ curves of 35% ^{13}C-labeled *i*PB1 form III at −20 °C and simulation curves (solid lines) with the shortest ^{13}C-^{13}C internuclear distances of 3.8 Å between the neighboring stems at both the *A* (red) and *B* sites (blue) and exponential T_2 values of 8.2 and 8.0 ms, respectively. (f) 2D DQ/SQ NMR spectrum of 35% ^{13}C-labeled *i*PB1 with $\tau_{ex} = 7.06$ ms at −20 °C.

^{13}C atomic coordinates and spin-relaxation process (T_2) at the two inequivalent sites (*A* and *B*).

To simulate DQ buildup curves at the two sites illustrated in Figs. 2(c) and 2(d), 13-spin systems, including one reference carbon plus the 12 closest surrounding atoms at distances less than 7.0 Å, were considered. A 35% labeling ratio of the methyl group produced statistically different spin systems, which were related to the interacting spin number, spin topology, and internuclear distance among the 13 sites, resulting in different buildup curves [Fig. S3]. The detailed calculation steps are described in the Supplemental Material [26]. The DQ curves at two sites calculated on the basis of the XRD results [28] induced slightly slower buildup than the experimental curves [Fig. S4(c)]. Thus, all of the coordinates were revised by shrinking the atomic

coordinates along all axes by approximately 5%. As a result, the DQ buildup curves simulated using the shortest internuclear distance of 3.8 Å and an exponential T_2 value of 8.2 and 8.0 ms at the A and B sites, respectively, reproduced the experimental results at both sites [Fig. 2(e)]. From the best-fit curves, the signals at 14.2 and 15.1 ppm were assigned to the A and B sites, respectively.

Two different explanations can account for the distance differences between the XRD and NMR results. One explanation involves imperfections in the NMR experiment, and the other involves inaccuracies in the XRD analysis. In fact, the packing structure for the well-known α form of isotactic poly(propylene) has been investigated by several groups. Natta *et al.* [30] reported that the shortest interstem CH_3 carbon-carbon distance was 4.2 Å, and this distance was later revised to 4.0 [31] and 3.8 Å [32]. Even XRD studies have reported differences in the interstem carbon-carbon distances in the range of 0.2–0.4 Å.

The spin networks at the A and B sites can also be confirmed by 2D ^{13}C-^{13}C DQ/SQ NMR spectra correlations [Fig. 2(f)], in which DQ correlations of identical and different chemical shifts lead to diagonal and off-diagonal peaks, respectively. Thus, the obtained two off-diagonal and two diagonal peaks correspond to the AB (BA) and the AA and BB correlations, respectively. The 2D peak volume ratios of $AA:AB:BA:BB$ are $19:34:34:13$. The relatively high volumes of the AB (BA) correlations are attributed to the first to the third closest distances at both sites. The fourth closest distances at the A (4.3 Å) and B sites (4.7 Å) arise from the interstem AA and BB correlations, respectively [see Figs. 2(c) and 2(d)]. These differences result in an AA peak volume that is larger than the BB volume and can also generate distinct differences in the DQ buildup curves between the A and B sites, as shown in Fig. 2(e). The refined atomic coordinates of the CH_3 group, internuclear distances [Figs. 2(c) and 2(d)], and T_2 values were further used to analyze the chain trajectory of the isolated ^{13}C-labeled chains in the single crystals.

In the case of ^{13}C-labeled chains blended with non-labeled chains, the compositional dependence of the DQ buildup curves confirmed that the individual ^{13}C-labeled chains were mixed with nonlabeled chains at stem levels [Fig. S5]. The blend including a 10 wt % labeled sample was used for the chain trajectory analysis. The experimental DQ buildup curves are displayed as red (A site) and blue (B site) open circles in Figs. 3(a)–3(d). Interestingly, the A site results ($\xi_{max} = 16\%$ at $=7.06$ ms) were almost consistent with those of the B site. Under the assumption that secondary nucleation dominates the CF process, four plausible CF models with different spin interactions were initially constructed without any morphological constraint on the folding directions. We designated these models as an isolated chain (CF0), a chain-folding A model (CFA) along (100), a CFB along
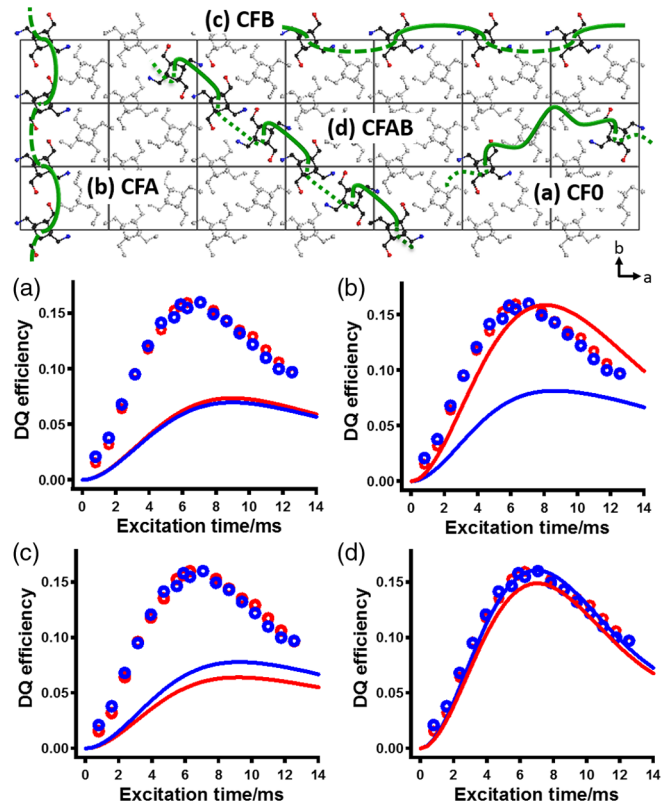
FIG. 3 (color online). Various CF models as 2D clusters and the corresponding simulated DQ NMR of *i*PB1 form III at $T_c = 50°$C: (a) CF0, (b) CFA, (c) CFB, and (c) CFAB models. The red (A site) and blue (B site) solid curves are the calculated results of (a) CF0 and are based on $\langle n \rangle = 13$ and (b) CFA with $\langle F_{CFA} \rangle = 100\%$, (c) CFB with $\langle F_{CFA} \rangle = 100\%$, and (d) CFAB with $\langle F_{CFA} \rangle = 90\%$ under the assumption of CF0 contributing to DQ efficiency as the remaining fraction 100-$\langle F \rangle$%. The red (A site) and blue (B site) open circles are the experimental DQ buildup curves of ^{13}C-labeled *i*PB1 chains blended with nonlabeled chains (1/9).

(010), and a CFAB along (110). We compared the overall DQ curves at the two sites with the simulated curves based on each CF model. Notably, the ^{13}C-^{13}C DQ simulated results for all chain trajectories included statistical inter-chain effects.

The isolated stem generated only internuclear inter-actions within the same stem, including the maximum 3 spins at distances less than 7.0 Å, whereas statistical interchain effects dominated buildup curves lower than the experimental ones shown in Fig. 3(a). The detailed spin combinations for all of the models are displayed in Fig. S6. In the different CF models, the reentrance sites, as well as the $\langle n \rangle$ and $\langle F \rangle$ values, significantly influenced DQ efficiency, with the greater heights of the calculated buildup curves at either A or B adjusted to the same levels as the experimental curve by changing the $\langle F \rangle$ value. When $\langle F \rangle$ does not equal 100%, the remainder of the fraction is assumed to result from the isolated stem structures.
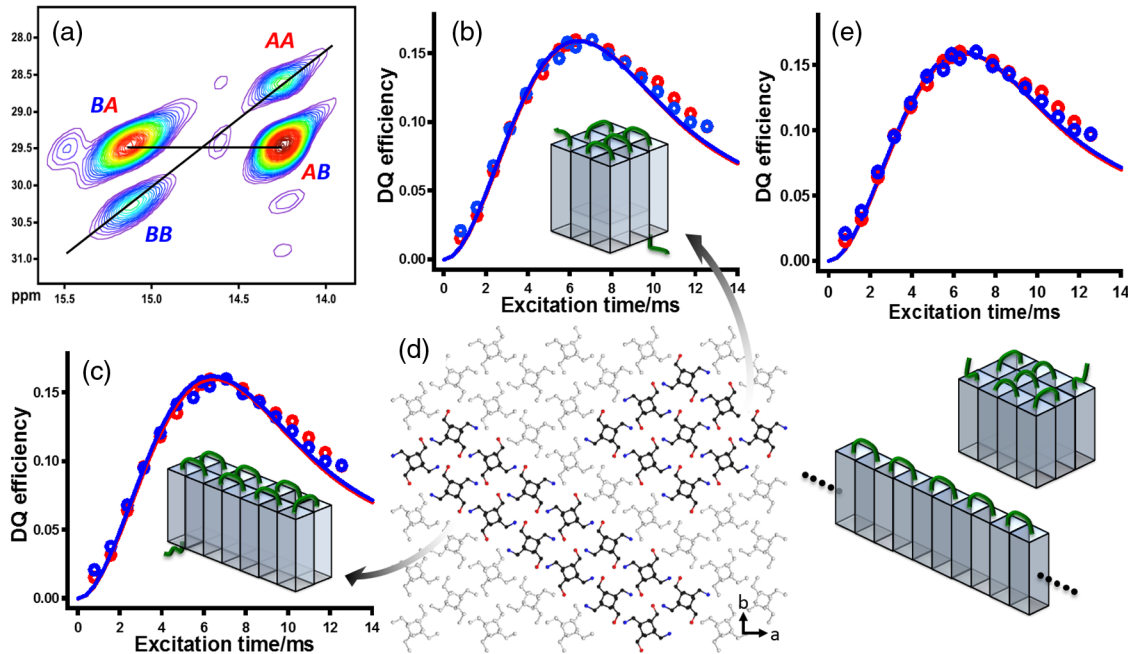
FIG. 4 (color online).   (a) 2D DQ/SQ NMR spectrum of ^{13}C-labeled iPB1 blended with nonlabeled chains (1/9) with $\tau_{ex} = 7.06$ ms; (b) and (c) show cluster models and DQ buildup curves of 10 wt % ^{13}C-labeled iPB1 blend in single crystals at $T_c = 50\,°C$. The red (A site) and blue (B site) open circles are the experimental curves. The red (A site) and blue (B site) solid lines were calculated on the basis of (b) $\langle F \rangle = 70\%$ and $\langle n_{stem} \rangle = 9$ and (c) $\langle F \rangle = 70\%$ and $\langle n_{stem} \rangle = 14$. (d) 2D molecular views of the $\langle n_{stem} \rangle = 9$ and 14 cluster models. (e) Mixture model of 2D (CFAB with $\langle F \rangle = 15\%$ and $\langle n \rangle = 13$) and 3D ($\langle F \rangle = 55\%$ and $\langle n_{stem} \rangle = 12$, 3 layers) clusters, including CF0 with $\langle F \rangle = 30\%$. The illustration represents a 2D and a 3D cluster.

In the CFA model, the calculated buildup curve at the A site assuming $\langle F \rangle = 100\%$ and $\langle n \rangle = 13$ possessed a similar height compared to the experimental data, but generated a slower buildup curve. In addition, a large difference was observed between the experimental and calculated curves for the B site. For the CFB model, both sites produced much lower buildup curves than the experimental results. Thus, we easily rejected these two models. In the CFAB model, the CF direction was parallel to the growth face of the single crystals. This structure is believed to be the relevant CF structure in form III single crystals [33]. Under the assumption of $\langle F \rangle = 90\%$ and $\langle n \rangle = 13$, the calculated curve at the B site was close to the experimental data. However, the calculated curve at the A site was evidently lower than the experimental result. Similarly, an insufficient spin network at the A site was also confirmed by the 2D DQ/SQ NMR spectrum shown in Fig. 4(a). The peak volume ratios of $AA\!:\!AB\!:\!BA\!:\!BB$ were observed to be $14\!:\!36\!:\!36\!:\!14$. The ^{13}C-^{13}C shortest internuclear distance between the AA sites was 6.2 Å. This longer distance did not result in the same peak volume as the BB correlation, which exhibited a shortest internuclear distance of 4.7 Å [Fig. S6]. The observed diagonal peak areas, as well as the DQ buildup curves at both sites refuted the CFAB model in a single layer as a proper structure.

None of the linear models tested here could reproduce the experimental data, although CFAB reproduced the

experimental results more closely than the other two models. To achieve the same ξ values at the A and B sites, similar spin networks at both sites such as those in the chain packing of ^{13}C-labeled homopolymers are necessary. Thereby, several 3D stem clusters generated via chain folding along (110) and $(1\bar{1}0)$ were further tested. The cluster consisting of four stems demonstrated that the calculated DQ buildup curve at the A site was insufficient. For the cluster with nine stems in three layers, as shown in Fig. 4(b), the calculated curve at the A site exhibited intensities almost completely consistent with those of the B site, and $\langle F \rangle = 70\%$ was able to successfully reproduce the experimental data at both sites. In addition, fourteen stems in two layers and twelve stems in three layers reproduced the experimental data when the $\langle F \rangle$ value was adjusted to 70% and 65%, respectively. The former result is shown in Fig. 4(c). These results indicate that 3D cluster models including nine to fourteen stems reproduced the experimental DQ buildup curves at both sites.

In recent molecular dynamics simulations [5–7], single chains were predicted to induce self-folding without a growth front, with the folded clusters further aggregating with each other in dilute solutions. In the latter case, the chains at the vicinity of the crystal surface were also reeled in, and CF events on the growth front were simultaneously observed. Thus, we considered the simultaneous deposition of the individual chains and 3D clusters. Assuming the

deposition of both chains and clusters on the growth front along (110), mixed models of 2D (CFAB) and 3D clusters composed of whole or partially folded chains finally tested. Several combinations of clusters with slightly different $\langle n \rangle$ and $\langle F \rangle$ values might be possible. One mixed model with a 2D CFAB cluster ($\langle F \rangle = 15\%$ and $\langle n \rangle = 13$) and 3D clusters of 3 layers ($\langle F \rangle = 55\%$ and $\langle n_{stem} \rangle = 12$) reproduced the experimental data, as shown in Fig. 4(e). The insufficient resolution of the DQ buildup curves was unable to distinguish the 3D cluster models from the mixed models. Nevertheless, the important finding is that the 3D cluster is the dominant structure in both models. The determined conformation for the folded chains in this study contradicts the secondary nucleation hypothesis. Hence, the self-folding of the chains in the precrystallization stage can be reasonably concluded to be the initial step. The clusters are subsequently deposited on the growth front [Fig. 1(b)]. Further kinetic effects on the CF structure may be of interest. Structural differences were not detected, even under rapid quenching to $0\,°C$ [see Fig. S7]; this result is consistent with the results of our former work on iPB1 form I [22].

In summary, spatial proximities between ^{13}C label positions as detected by DQ NMR at multiple sites proved the 3D conformation of the folded chains in form III single crystals, which supports the hypothesis that crystallization is dominated by two-step mechanisms involving the formations of 3D clusters via self-folding and their deposition on the growth front. The proposed crystallization mechanism is consistent with theoretical bundle [4] and aggregation models [5].

---

*Corresponding author.
miyoshi@uakron.edu

[1] L. Mandelkern, *Crystallization of Polymers* (McGraw-Hill, New York, NY, 1964).
[2] J. I. Lauritzen, Jr and J. D. Hoffman, J. Res. Natl. Bur. Stand., Sect. A **64A**, 73 (1960).
[3] J. D. Hoffman and R. L. Miller, Polymer **38**, 3151 (1997).
[4] G. Allegra and S. Meille, Adv. Polym. Sci. **191**, 87 (2005).
[5] J. Zhang and M. Muthukumar, J. Chem. Phys. **126**, 234904 (2007).
[6] P. Welch and M. Muthukumar, Phys. Rev. Lett. **87**, 218302 (2001).
[7] C. Liu and M. Muthukumar, J. Chem. Phys. **109**, 2536 (1998).
[8] S. J. Spells and D. M. Sadler, Polymer **25**, 739 (1984).
[9] J. M. Guenet, D. M. Sadler, and S. J. Spells, Polymer **31**, 195 (1990).
[10] K. R. Reddy, K. Tashiro, T. Sakurai, and N. Yamaguchi, Macromolecules **41**, 9807 (2008).
[11] J. C. Wittmann and B. Lotz, J. Polym. Sci., Polym. Phys. Ed. **23**, 205 (1985).
[12] J. Kumaki, T. Kawauchi, and E. Yashima, J. Am. Chem. Soc. **127**, 5788 (2005).
[13] N. Mullin and J. K. Hobbs, Phys. Rev. Lett. **107**, 197801 (2011).
[14] K. Liu, Y. Song, W. Feng, N. Liu, W. Zhang, and X. Zhang, J. Am. Chem. Soc. **133**, 3226 (2011).
[15] K. Schmidt-Rohr, W. Hu, and N. Zumbulyadis, Science **280**, 714 (1998).
[16] M. A. Mehta, M. T. Eddy, S. A. McNeill, F. D. Mills, and J. R. Long, J. Am. Chem. Soc. **130**, 2202 (2008).
[17] T. Gullion, K. Yamauchi, M. Okonogi, and T. Asakura, Macromolecules **40**, 1363 (2007).
[18] S. P. Brown and H. W. Spiess, Chem. Rev. **101**, 4125 (2001).
[19] K. Nomura, K. Takegoshi, T. Terao, K. Uchida, and M. Kainosho, J. Am. Chem. Soc. **121**, 4064 (1999).
[20] F. Castellani, B. van Rossum, A. Diehl, M. Schubert, K. Rehbein, and H. Oschkinat, Nature (London) **420**, 98 (2002).
[21] Y.-l. Hong, T. Koga, and T. Miyoshi, Macromolecules **48**, 3282 (2015).
[22] Y.-l. Hong and T. Miyoshi, ACS Macro Lett. **2**, 501 (2013).
[23] Y.-l. Hong and T. Miyoshi, ACS Macro Lett. **3**, 556 (2014).
[24] D. Maring, M. Wilhelm, H. W. Spiess, B. Meurer, and G. Weill, J. Polym. Sci., Part B: Polym. Phys. **38**, 2611 (2000).
[25] T. Miyoshi, S. Hayashi, F. Imashiro, and A. Kaito, Macromolecules **35**, 2624 (2002).
[26] See Supplemental Material at http://link.aps.org/supplemental/10.1103/PhysRevLett.115.168301 for sample preparation, NMR experimental conditions, and simulation, which includes Ref. [27–29].
[27] M. Veshtort and R. G. Griffin, J. Magn. Reson. **178**, 248 (2006).
[28] T. Karlsson, J. M. Popham, J. R. Long, N. Oyler, and G. P. Drobny, J. Am. Chem. Soc. **125**, 7394 (2003).
[29] G. Cojazzi, V. Malta, G. Celotti, and R. Zannetti, Makromol. Chem. **177**, 915 (1976).
[30] G. Natta and P. Corradini, Nuovo Cimento **15**, 52 (1960).
[31] Z. Mencik, J. Macromol. Sci., Part B: Phys. **6**, 101 (1972).
[32] M. Hikosaka and T. Seto, Polym. J. **5**, 111 (1973).
[33] B. Lotz and A. Thierry, Macromolecules **36**, 286 (2003).